Near-Inertial Wave Interactions with Mean Flow and Bottom Topography near Caryn Seamount

ERIC KUNZE AND THOMAS B. SANFORD

Applied Physics Laboratory and School of Oceanography, University of Washington, Seattle, WA 98105

(Manuscript received 4 December 1984, in final form 23 July 1985)

ABSTRACT

Velocity measurements near Caryn Seamount in the Sargasso Sea reveal intensified mean and near-inertial motions in the upper ocean. Embedded in a regional eastward flow is an anticyclonic eddy that appears to be tied to the topography. An energetic downward-propagating near-inertial wave packet is found at the eddy's base. This wave appears to be trapped in the eddy, undergoing critical-layer amplification as it tries to leave. Near the bottom, enhanced upgoing near-inertial wave energy is found within 1000 m of the top of the seamount.

1. Introduction

Extensive velocity profiling has revealed numerous instances of strong, isolated packets of downward-propagating near-inertial energy (Leaman and Sanford, 1975; Johnson et al., 1976; Pinkel, 1983; Kunze and Sanford, 1984; D'Asaro, 1984), but few examples of energetic, upgoing near-inertial waves. Upward-propagating internal waves might be generated by mean flow or tidal motion over rough bottom topography (Henderschott, 1973; Bell, 1975). Eriksen (1982) demonstrated that internal waves with characteristic slopes comparable to the bottom slope can be amplified on reflection off bathymetry. Defant (1961) observed energetic inertial oscillations in a Taylor column above the "Altair" cone, and both Leaman (1976) and Fu (1981) reported more upward-propagating inertial energy present over rough topography than over a smooth. Strong anomalies in higher frequency internal waves have been measured around Muir Seamount (Wunsch and Webb, 1979) and Bermuda (Johnson and Sanford, 1980) but without enhancement of near-inertial energy.

In an effort to find topographically-influenced inertial motions, a series of velocity profiles was collected over an isolated seamount. This data set is used to describe the spatial structure of the mean flow and internal waves on and around the peak.

2. The setting and data

Caryn Seamount rises abruptly to a relatively flat top at 2852 m depth, about 2100 m above the surrounding abyssal plain (4950 m) (Fig. 1). The seamount lies at 36°40'N, 68°W, at the juncture of the Sohm Abyssal Plain and the continental rise south of New England. Other than the very gentle grade of the rise, there are no major topographic perturbations within hundreds of kilometers. This isolation should make the peak an ideal site for unambiguous identification of topographically-influenced waves.

The data set consists of seven absolute velocity profiles from the surface to the bottom at three sites (AVP 380–386) and 22 relative velocity profiles (XCP 100–121) to 900 m deployed in a cross-shaped array (Fig. 1). The absolute velocity profiles were collected with the Absolute Velocity Profiler (Sanford et al., 1985), the relative velocity profiles with expendable velocity profilers (Sanford et al., 1982). Casts with a NBIS Mk 3 CTD were made at the AVP drop sites.

The density structure at the site consists of several distinct regimes (Fig. 2). Below a 30-m thick surface mixed layer, a sharp seasonal pycnocline caps the "18°C water" (Worthington, 1959) spanning 100–550 m. Below 550 m, the permanent pycnocline extends to 1200 m with typical Sargasso Sea stratification found beneath. The buoyancy frequency has its principal maximum of 8×10^{-3} s^{-1} in the upper 100 m, values as low as 2×10^{-3} s^{-1} in the 18°C water, a secondary maximum of 4.5×10^{-3} s^{-1} between 600 and 1000 m, and a value of 10^{-3} s^{-1} in deeper water.

3. Analysis

The velocity profiling revealed strong mean and near-inertial motions in the vicinity of the seamount. In Fig. 3, AVP profiles taken half an inertial period apart are used to separate the mean flow (a, b) from near-inertial motions (c). A surface-intensified mean flow of 20–30 cm s^{-1} extends to the base of the 18°C water. The mean shears are largest in the main pycnocline (600–1000 m) where the buoyancy frequency is also high (Fig. 2). Flows below the main pycnocline are 5–10 cm s^{-1}, weakening with depth.

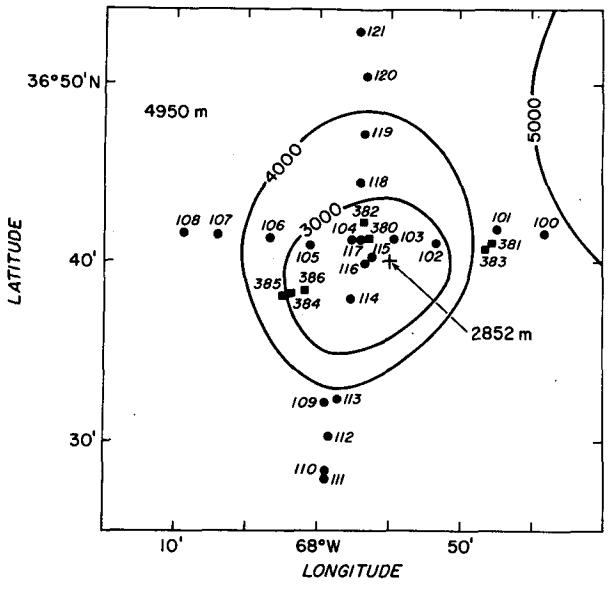

FIG. 1. Bathymetry and drop positions over Caryn Seamount. Bottom contours are in meters. The solid circles are locations of expendable current profiles; the squares denote absolute velocity profiles. CTD casts were also made at the AVP drop sites.

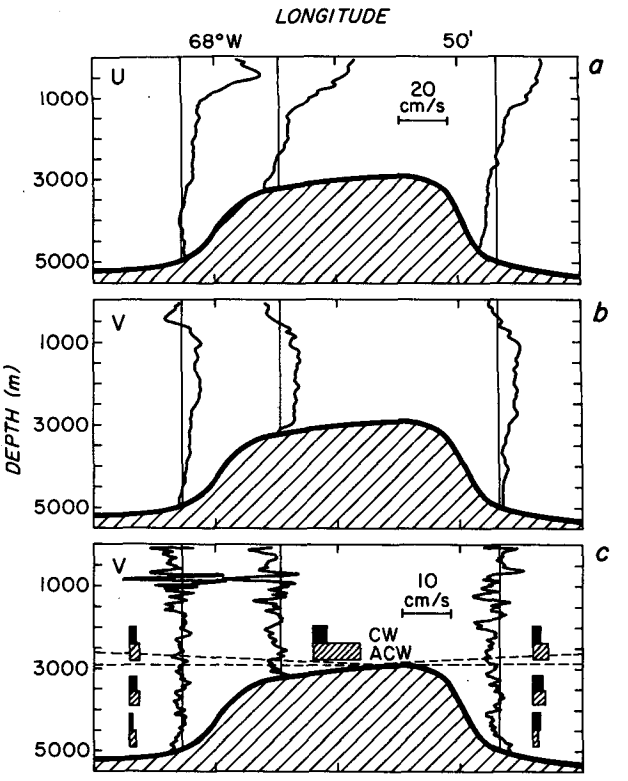

FIG. 3. Absolute velocity profiles over the seamount. Half-inertial period pairs were used to separate the mean (a, b) and near-inertial wave (c) motions. The mean profiles have also been smoothed with a running 50-m boxcar average. The vertical lines represent zero velocity. In (c), only the north component v is plotted. The bars below 1700 m in (c) are the WKB-normalized downgoing (solid) and upgoing (hatched) energy pairs in 1500-m bins. The dashed lines bracket the range of slopes for upward-propagating near-inertial characteristics.

Strong near-inertial motions with vertical wavelengths of 100 m are embedded in the pycnocline (600–1000 m) above and to the west of the seamount (Fig. 3c). These waves are downward-propagating, as revealed by their clockwise-with-depth velocity structure, not shown (Leaman and Sanford, 1975). This downward propagation indicates that they did not originate at the bottom but are likely wind-generated. Profiles to the east of the seamount were far less energetic on these scales. These motions will be discussed in greater detail in the next section.

Below 1700 m the bars in Fig. 3c indicate the WKB-normalized clockwise-with-depth (downgoing) and anticlockwise-with-depth (upgoing) energies in 1500 m intervals. Upward-propagating energy was most intense on top and to either side of the summit along near-inertial characteristics, where *near-inertial* is taken to signify $f < \omega_0 < 1.1f$. [Note: corrections to the characteristics (Fig. 3c) to account for the fact that waves on opposite sides of the peak propagate either with or against the current are negligible. For the mean flow to make a factor of 2 difference between the up- and downstream characteristic slopes, the waves' horizontal wavelengths would have to be an order of magnitude smaller than typically observed in the pycnocline.] Upgoing energy also dominated in deeper waters on the sides of the seamount but less dramatically.

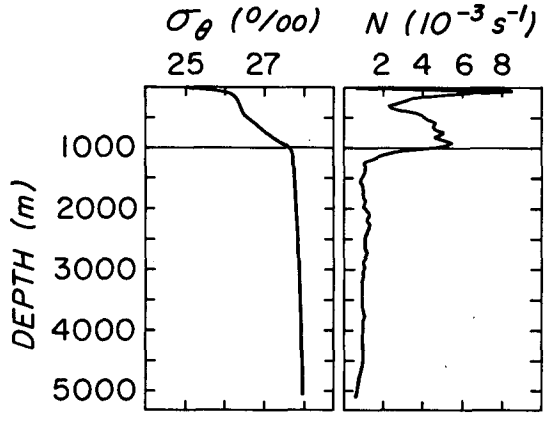

FIG. 2. The density and buoyancy frequency profiles over the seamount. A layer of "18°C water" extends from 100 to 550 m.

This excess "upward-propagating" wave energy in the vicinity of the seamount points to a topographic cause. We will confine our attention to near-inertial waves since they dominate the internal wave velocity field and because higher frequency waves should exhibit equipartition of energy between the clockwise- and anticlockwise-with-depth components. Unfortunately, the limited number of deep profiles at each site prevents

unambiguous identification of the frequency of fluctuations below 1000 m. In favor of the near-inertial assumption, half-inertial period pair-sums have far less high wavenumber variability than pair-differences even before the smoothing in Fig. 3a and 3b. This also rules out bottom generation by the mean flow since waves generated by that mechanism would have zero Eulerian frequencies. Generation by barotropic tides cannot be eliminated, however; barotropic fluctuations were 3–4 cm s^{-1} on the sides of the peak and 7 cm s^{-1} on the summit.

One possible mechanism for topographic enhancement of near-inertial waves is bottom reflection. Eriksen (1982) demonstrated that an internal wave propagating upslope would be amplified upon reflection off sloping bathymetry as a consequence of the requirement of zero energy flux normal to the bottom. Amplification occurs for waves with characteristic slopes comparable to the bottom slope and is strongest for waves propagating normal to isobaths. For these waves the ratio of reflected to incident energies is

$$\frac{E_r}{E_i} = \left(\frac{k_{z_r}}{k_{z_i}}\right)^2 = \left\{\frac{[(\omega^2 - f^2)^{1/2} + N\tan\theta]}{[(\omega^2 - f^2)^{1/2} - N\tan\theta]}\right\}^2$$

where θ is the bottom slope, and k_{z_i} and k_{z_r} are the incident and reflected vertical wavenumbers. For a more general reflection equation valid for waves with a component of propagation alongslope, the reader is referred to Eriksen (1982). The point we wish to make is that the ratio of reflected to incident energy will be greater than one for positive $\tan\theta$ and will be very large for $N\tan\theta \approx (\omega^2 - f^2)^{1/2}$. Waves with characteristics steeper than the bathymetry are reflected vertically, those with gentler characteristics horizontally. In favor of the reflection hypothesis, the enhancement of anticlockwise-with-depth (upgoing) relative to clockwise-with-depth waves is confined to vertical wavelengths less than 500 m (100 m WKB-normalized for $N_0 = 5 \times 10^{-3}$ s^{-1}) as would be expected for the amplified reflected waves being scattered to high wavenumber.

Wunsch and Webb (1979) suggested that, despite near-bottom enhancement, the bottom might not be a source of internal waves. If this is assumed to be the case, then all waves must originate at the surface and initially be propagating downward. Amplification near sloping bathymetry is a purely kinematic effect resulting from conservation of energy flux. The reflected waves have smaller group velocities because of their higher wavenumbers. In Table 1, the theoretical frequency bands for which reflected waves are at least twice as energetic as the incident wave are given for the slopes on the summit and sides of the peak. The near-inertial wave frequency peak was found to lie in $(1.01–1.09)f$ by Fu (1981) and in $(1.03–1.07)f$ by D'Asaro and Perkins (1984). Thus, on the summit, vertically-reflected (that is, upgoing) near-inertial waves should be intensified, consistent with the features observed on and to either side of the summit in Fig. 3c. On the sides, waves reflected horizontally should be magnified, retaining their downward energy propagation. This mechanism does not explain the enhanced anticlockwise energy on the sides of the seamount. It should be noted, however, that the topography of Caryn Seamount is not well known. The sides may in fact be much steeper so that near-inertial waves reflect without amplification. The enhancement of upgoing energy might then be due to weaker slopes at the base. Alternatively, bottom generation by the barotropic diurnal tide may play some role as already suggested.

TABLE 1. Frequency bands for which the ratio of reflected to incident energy is greater than two over the seamount.

Reflection	Summit ($\tan_\theta = 0.01$)	Sides ($\tan_\theta = 0.08$)
Vertical	$\omega = (1.01–1.24)f$	$\omega = (1.5–3.0)f$
Horizontal	$\omega = (1.004–1.01)f$	$\omega = (1.02–1.5)f$

Because the AVP profiles revealed an energetic near-inertial wave packet at 600–1000 m, a survey with XCPs was undertaken to delineate the spatial structure of the wave and the mean flow field. The positions of the XCP drops are given in Fig. 1. Figure 4 presents sections of velocity profiles taken along the east–west (a) and north–south (b) legs. The dashed lines represent the least-squares fit to a second degree polynomial. The fit is dominated by geostrophic shear. The more energetic of the deviations from the fit are due mainly to near-inertial motions with vertical wavelengths O(100 m).

The mean flow exhibits considerable variability over the site. As is shown in Fig. 5, there is a general eastward flow to the north and east, and an anticyclonic eddy in the southwest. The direction and magnitude of these upper ocean currents were derived independently for each profile. Three analysis methods were employed: (i) least-squares fitting a second degree polynomial to the profiles (Fig. 4); (ii) computing vertically-averaged velocities in the 18°C water (100–550 m) relative to the permanent pycnocline (550–900 m); and (iii) rotating the profiles into a reference frame where the velocity variance is maximized along one axis (minimized along the other), and then estimating the velocity in the 18°C water relative to 900 m. All these methods revealed the same structure. In Fig. 5, the mean flow at 800–900 m as measured by the AVPs, which was the same at all three sites [$(U, V) = (15, 5)$ cm s^{-1}], has been added to the results of method (iii). Because most of the profiles are relative, there is some uncertainty about the absolute magnitudes of the flows. Nevertheless, the similarity of the flow at 800–900 m for all 3 AVP sites suggests that the velocity structure is correct.

An alternative presentation of the velocity structure is given in Fig. 6d, e which displays the relative 18°C

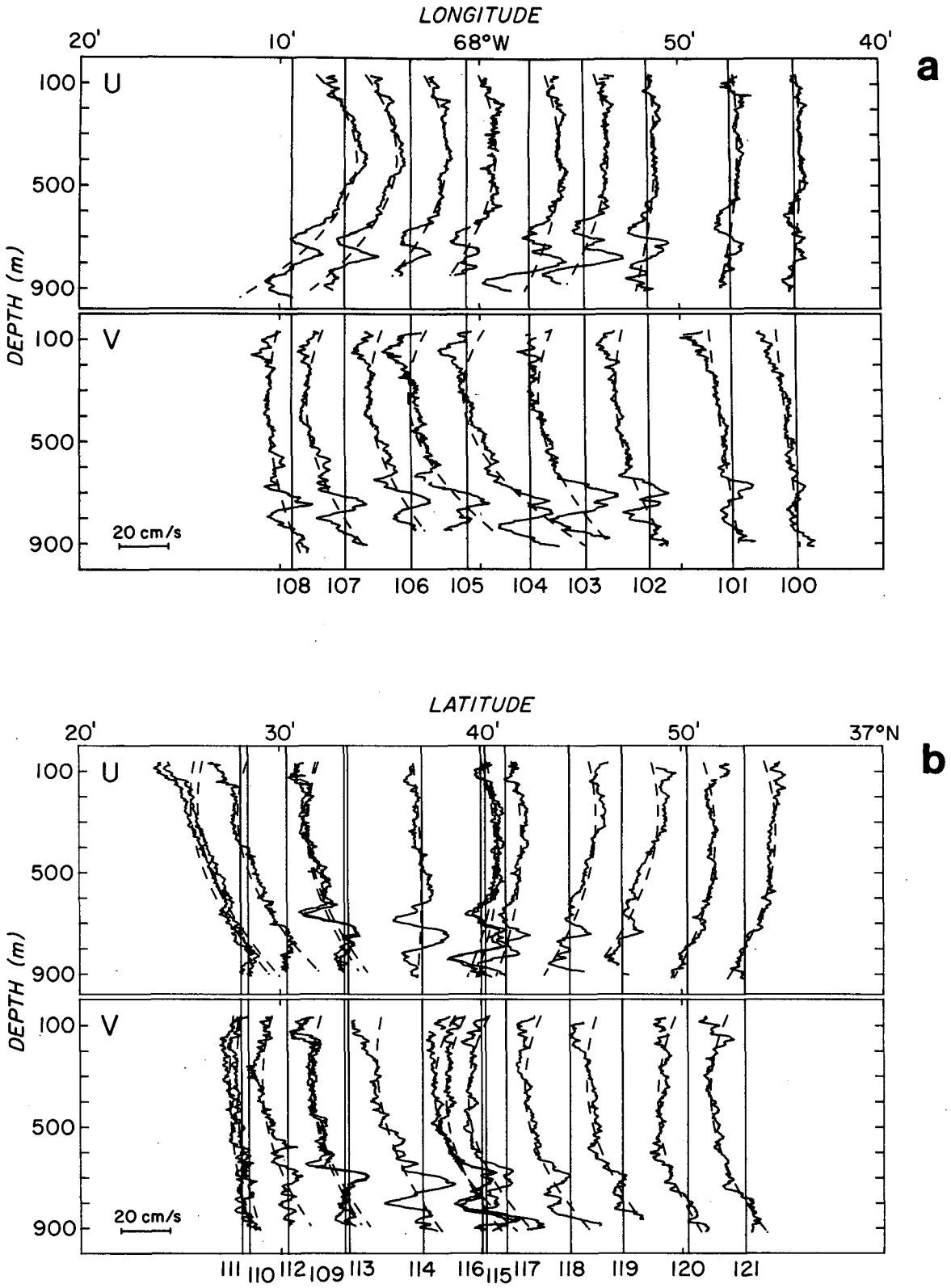

FIG. 4. Longitudinal (a) and meridional (b) sections of XCP velocity profiles. The profiles are relative, plotted so that the flow averaged over 600–800 m is zero. For each leg, the geomagnetic east velocity component U is in the upper half, and the north component V is in the lower half. XCP 109 and 113 are at the same location but separated by 1 hour. The dashed curves represent second-degree polynomial fits which represent the steady flow structure.

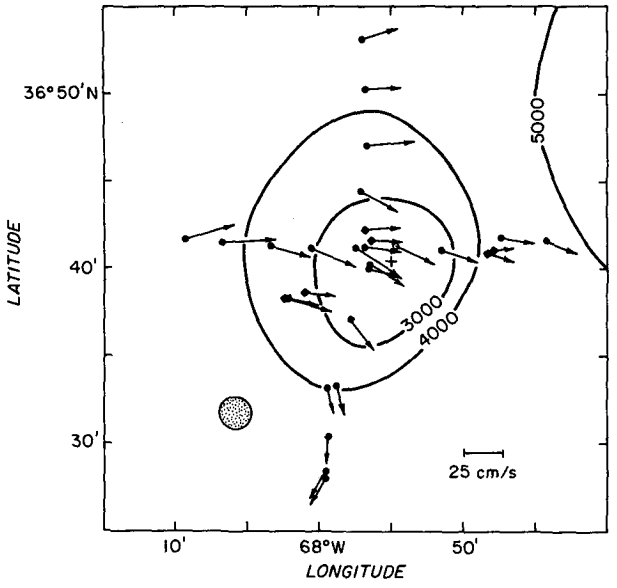

FIG. 5. The structure of the flow in the 18°C water. The XCP-measured velocities over 800–900 m in the pycnocline have been adjusted to the value measured by the AVPs at all three sites, $(U, V) = (15, 5)$ cm s^{-1}. An anticyclonic eddy occupies the southwest corner of the survey. Its center, inferred from chords of the velocity vectors in the west and south branches under the assumption that the eddy is at rest with respect to the seamount, is indicated by the stippled circle. Away from the eddy, the background flow in the north and east branches is 25 cm s^{-1} directed almost due east.

water velocities from method (iii) along each leg. The slopes of the velocities in Fig. 6d—*left* and 6e—*right* are the strains $\partial U/\partial x$ and $\partial V/\partial y$ respectively. The decrease in the U-component to the east suggests confluence that must be balanced by an increase in the V-component to the north. This balance is evident in the structure of the background of the anticyclonic eddy in Fig. 5. The slopes in Fig. 6d–*right* and 6e–*left* are the vorticity components $\partial U/\partial y$ and $\partial V/\partial x$ which are negative south of 36°45'N and west of 68°W.

Interactions with topography are not limited to internal wave enhancement; stratified Taylor columns have been observed above peaks (Defant, 1961; Owens and Hogg, 1980; Gould et al., 1981; Roden, 1985). Swaters and Mysak (1985) found that the column will be surface- rather than bottom-intensified if the impinging current is strongest at the surface as appears to be the case for the flow observed here. This mechanism may be responsible for the warm eddy southwest of the seamount. Richardson (1980) also inferred topographic generation of warm, anticlockwise eddies from buoy tracks near the Corner Rise Seamounts. If the eddy is topographically-forced, its center must be at rest. This center has been inferred from the velocity structure in the south and west branches of the survey using intersections of velocity chords. Its position is indicated in Fig. 5 by the stippled circle.

It is also possible that this feature is part of the upper ocean eddy field of the Sargasso Sea that is being advected over the seamount. However, if the current along the north and east branches is removed from all the values in Fig. 5, the pattern of flow loses its eddylike character with velocities in the south branch becoming much more intense than in the other branches. This could only be possible if there is a cold, cyclonic eddy to the south of the array. As the temperature structure (Fig. 6c) suggests a warm core in the south and west branches consistent with the eddy structure inferred for a center at rest, we conclude that the eddy is interacting with the seamount and is better described in a coordinate system fixed to the peak (as is shown in Fig. 5) than one moving with the background flow. Taking this to be the case, the data in Fig. 6 may be presented more appropriately as radial sections in eddy-centered coordinates. This is done in Fig. 7. The eddy is warmer than the surrounding ocean (Fig. 7a); cooler waters were found to the north, east and south. The core has vorticity $\zeta = -0.7f$ (Fig. 7d) and negligible radial velocities. Beyond a 25 km radius, the velocities probably reflect the background flow and so should not be considered as part of the eddy. Profiles containing excessive downward-propagating near-inertial wave energy are confined to the eddy (Fig. 7e).

4. Velocity finestructure

This section treats the downward-propagating near-inertial wavepacket at the base of the eddy between 600 and 900 m (Figs. 4, 6, and 7). In the 18°C water, where neither vorticity or mean flow have significant vertical gradients, WKB-normalized energy levels are far below canonical GM values (Fig. 6b), probably reflecting the weaker winds of summer (D'Asaro, 1984). Enhancement above the canonical level (Figs. 6f and 7e) is found only in the depth range of strong vertical gradients in the mean flow and vorticity (Fig. 3).

Kunze and Sanford (1984) reported intense downward-propagating near-inertial waves on the negative vorticity side of the North Pacific Subtropical Front. Enhancement has also been found in the California Current (Weller, 1985), a Sargasso Sea front (Mied et al., 1986), numerous warm-core rings by the authors, Lueck (personal communication, 1985) and Glenn (personal communication, 1985) and in a cold-core ring. Magaard (1968) has shown that mean flow vorticity ζ modifies the lower bound of the internal waveband from the planetary value of the Coriolis frequency f to an effective Coriolis frequency $f_{\text{eff}} = f + \zeta/2$. Physically, the wave feels the fluid's as well as Earth's rotation. This dependence of the lower bound of the internal waveband on mean vorticity implies that the internal waveband will be broader in regions of negative vorticity (Mooers, 1975). In these regions, waves with frequencies below f can exist which are unable to propagate into the surrounding irrotational ocean. Doppler-shifting can also trap those near-inertial waves prop-

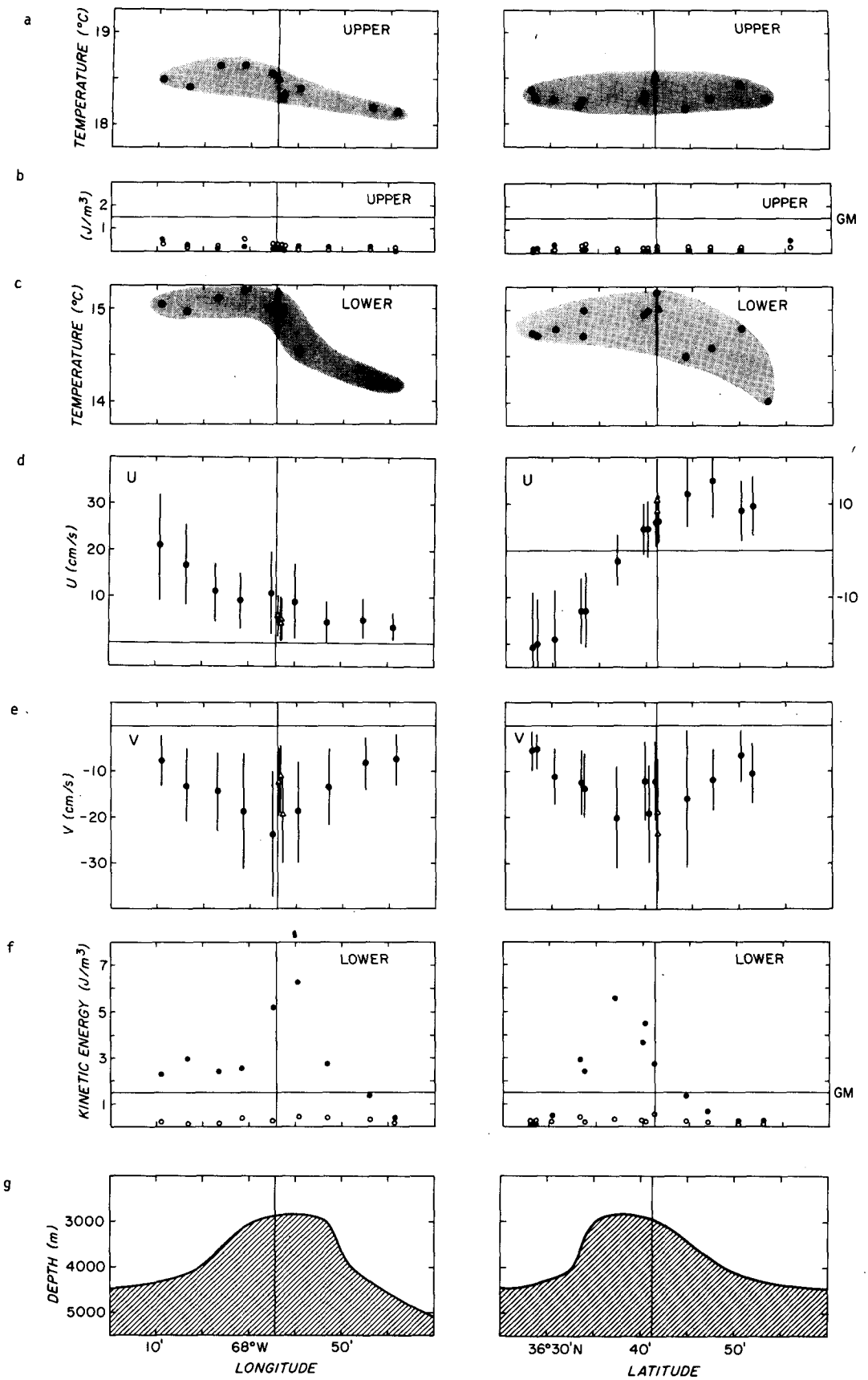

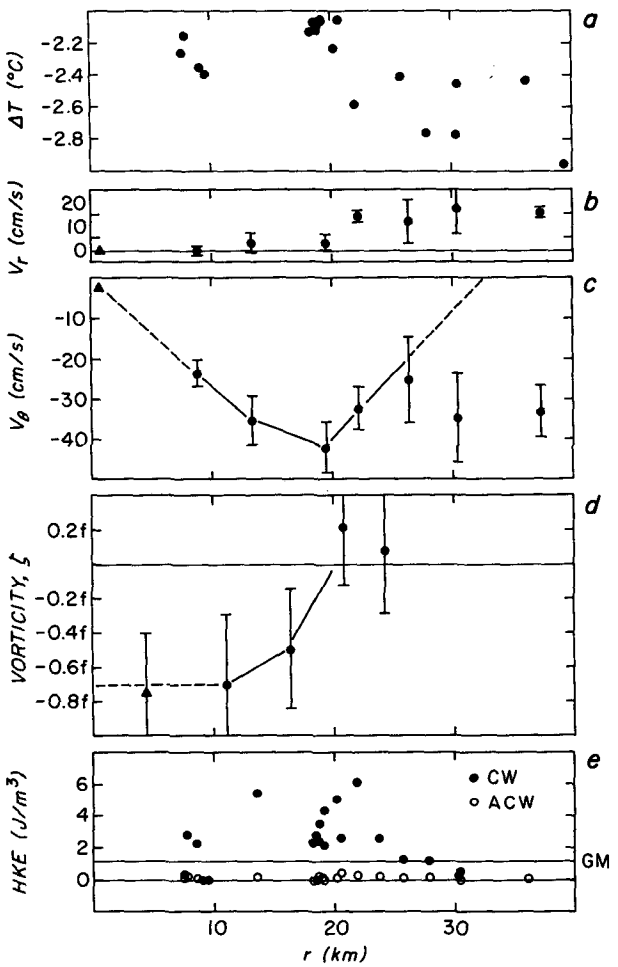

FIG. 7. Radial sections in eddy-centered coordinates of:

(a) the temperature difference between 600–800 m in the permanent pycnocline and 180–300 m in the 18°C water,

(b) radial flow V_r,

(c) azimuthal flow V_θ and

(d) vorticity = $\partial V_\theta/\partial r + V_\theta/r$ in the 18°C water, and

(e) downgoing (solid) and upgoing (open) near-inertial wave energies in the lower half of the XCP profiles.

In (b), (c) and (d) values have been averaged in overlapping radial bins while in (a) and (e) estimates from individual profiles are displayed. The triangles in panels (b), (c) and (d) are based upon the assumption that the eddy center is at rest. The eddy structure appears consistently in all the parameters plotted out to 20–25 km radius. Outside 25 km, the velocity structure is dominated by the background flow.

agating against the mean flow (Olbers, 1981). For both these effects, trapping takes the form of turning points in the horizontal (where the horizontal wavenumber passes through zero), and critical layers in the vertical (where the vertical wavelength shrinks and amplitude magnifies) (Kunze, 1985).

It is proposed that the energetic wave in this data set is trapped in the warm eddy. In Fig. 7, enhanced downgoing energy is associated with both the negative vorticity core and the velocity maximum, most strongly with the velocity maximum. The vertical variation of both vorticity and the Doppler shift favor critical-layer trapping of the wave as it travels downward. The negative vorticity of the core results in the lower bound of the internal waveband, $f_{\text{eff}} = f + \zeta/2$, being reduced in the 18°C water. As the vorticity becomes less negative with depth, the internal waveband narrows, pushing f_{eff} upward toward the intrinsic frequency of the wave, ω_0. And the Doppler shift also becomes less negative with depth (to be shown), forcing the intrinsic frequency ω_0 down toward f_{eff} as the wave tries to leave the eddy.

The profiles taken in the wave will be used along with the near-inertial wave dispersion relation to test the trapping hypothesis and the roles of negative vorticity and the Doppler shift. The intrinsic frequency ω_0 for near-inertial waves of the form $\exp[i(\mathbf{k}\cdot\mathbf{x} - \omega t)]$ propagating in geostrophic shear is given by

$$\omega_0 = \omega - (\mathbf{k}_H\cdot\mathbf{V}_H) \approx f + \zeta/2 + N^2k_H^2/(2fk_z^2) + (k_y\partial U/\partial z - k_x\partial V/\partial z)/k_z \quad (1)$$

(Kunze, 1985), where the Eulerian frequency ω is constant, $(\mathbf{k}_H\cdot\mathbf{V}_H)$ is the Doppler shift and N the buoyancy frequency. Each of the terms in (1) can be estimated from the data at hand.

If a single near-inertial wave dominates the energetic downgoing feature then it should be possible to determine its Eulerian frequency ω from the migration of peaks and troughs upward in profiles taken at the same position but different times (Leaman, 1976). For a wave propagating in a steady current, the Eulerian frequency ω (the frequency measured at a fixed point) is invariant, while the intrinsic frequency $\omega_0 = \omega - (\mathbf{k}\cdot\mathbf{V})$ is modulated by changes in the Doppler shift $(\mathbf{k}\cdot\mathbf{V})$ along the wave's path.

FIG. 6. East–west and north–south sections of:

(a) temperature averaged over 180–300 m.

(b) down- (solid symbols) and upgoing (open symbols) horizontal kinetic energy above 500 m depth. These values lie well below canonical GM values.

(c) temperatures averaged over 600–800 m in the main pycnocline. More horizontal variability is seen than in the 18°C water.

(d) east velocity U in the 18°C water relative to 900 m. The triangles are values from the other leg at the junction. The slope in the east–west section implies convergence west of 68°W. The slope in the north–south section implies negative vorticity between 36°30′N and 36°45′N.

(e) north velocity V in the 18°C water relative to 900 m.

(f) down- (solid symbols) and upgoing (open symbols) horizontal kinetic energy in the main pycnocline. Upgoing energies are similar to those in the 18°C water (b) while downgoing energies exceed GM values west of 67°52′W and between 36°35′ and 40′N.

(g) Bathymetry over the seamount.

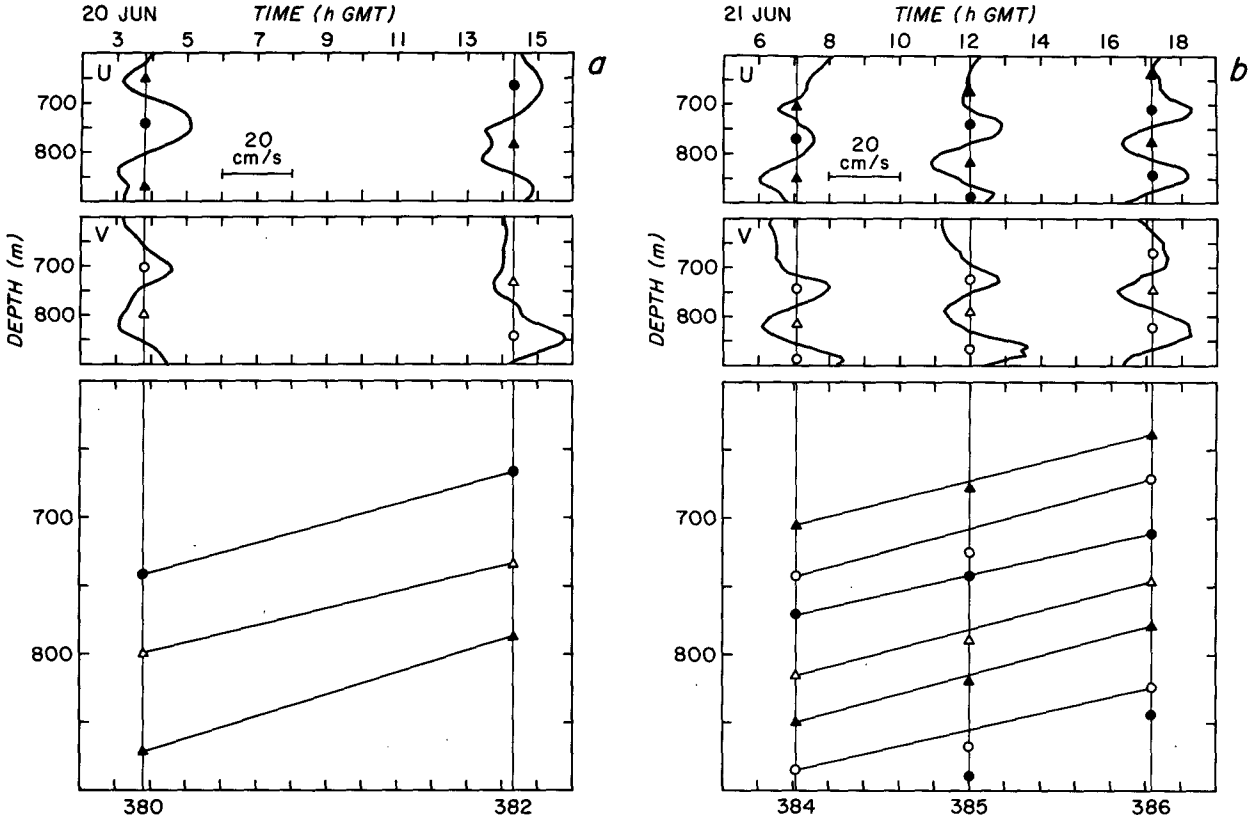

FIG. 8. Time series of the velocity structure of the energetic wavepacket at the two AVP sites. The east velocity component u is plotted in the upper panel, the north velocity component v in the mid-panel. The peaks and troughs in u and v are indicated by the symbols. These are combined in the lowermost panel. Only symbols appearing in more than one profile are repeated. For clockwise-with-depth near-inertial motions, phase propagates upward in time, allowing us to distinguish which peak is associated with which in 380/382. The upward phase propagation is unambiguously resolved for 384/385/386. The accompanying Table 2 gives the vertical wavelengths and frequencies associated with each extrema, as well as values computed after averaging the extrema depths in each profile together (bottom row).

Figure 8 and the accompanying Table 2 compare the depths of the peaks and troughs in profiles at the two AVP sites where the energetic packet was present.

TABLE 2. Vertical wavelengths and Eulerian frequencies estimated for individual peaks and troughs and for profile ensembles (the extrema depths in each profile were averaged together before computing the frequency).

	λ_z (m)	ω (f)
(a) Time series AVP 380/382 (Fig. 8a)		
Solid circle	220	0.65
Open triangle	250	0.49
Solid triangle	270	0.60
Ensemble	*230*	*0.60*
(b) Time series AVP 384/385/386 (Fig. 8b)		
Solid triangle	150	0.84
Open circle	130	1.04
Solid circle	140	0.81
Open triangle	150	0.90
Ensemble	*140*	*0.91*

Though all the extrema are shown in Fig. 8, only those above 800 m in all the profiles are used to estimate the frequency so that a single value of mean velocities U, V and buoyancy frequency N may be used later when computing the intrinsic frequency ω_0. Eulerian frequencies at the two sites are $0.6f$ and $0.9f$. Both these values are below f, but then the Eulerian frequency is not restricted to be above f; f (or f_{eff}) is only a lower bound on the intrinsic frequency ω_0. Of greater concern is the disparity between the two values which, as already indicated, is not what would be expected for a packet dominated by a single wave. The slopes $\Delta z/\Delta t$ in Fig. 8 are the same at the two sites but the vertical wavelengths differ. Estimates of the vertical wavelengths are very reliable and are consistent at each site (250 and 140 m). There is no reason why a wave's vertical wavelength should be fixed; in fact it should vary in a vertically-inhomogenous medium. Measurement problems are more likely to affect the accuracy of the slopes $\Delta z/\Delta t$. The disparities between the two frequencies amount to depth offsets of 20 m, larger than would be expected from the 5 m error in estimating the extrema depths. Note, however, that the AVPs at each site were

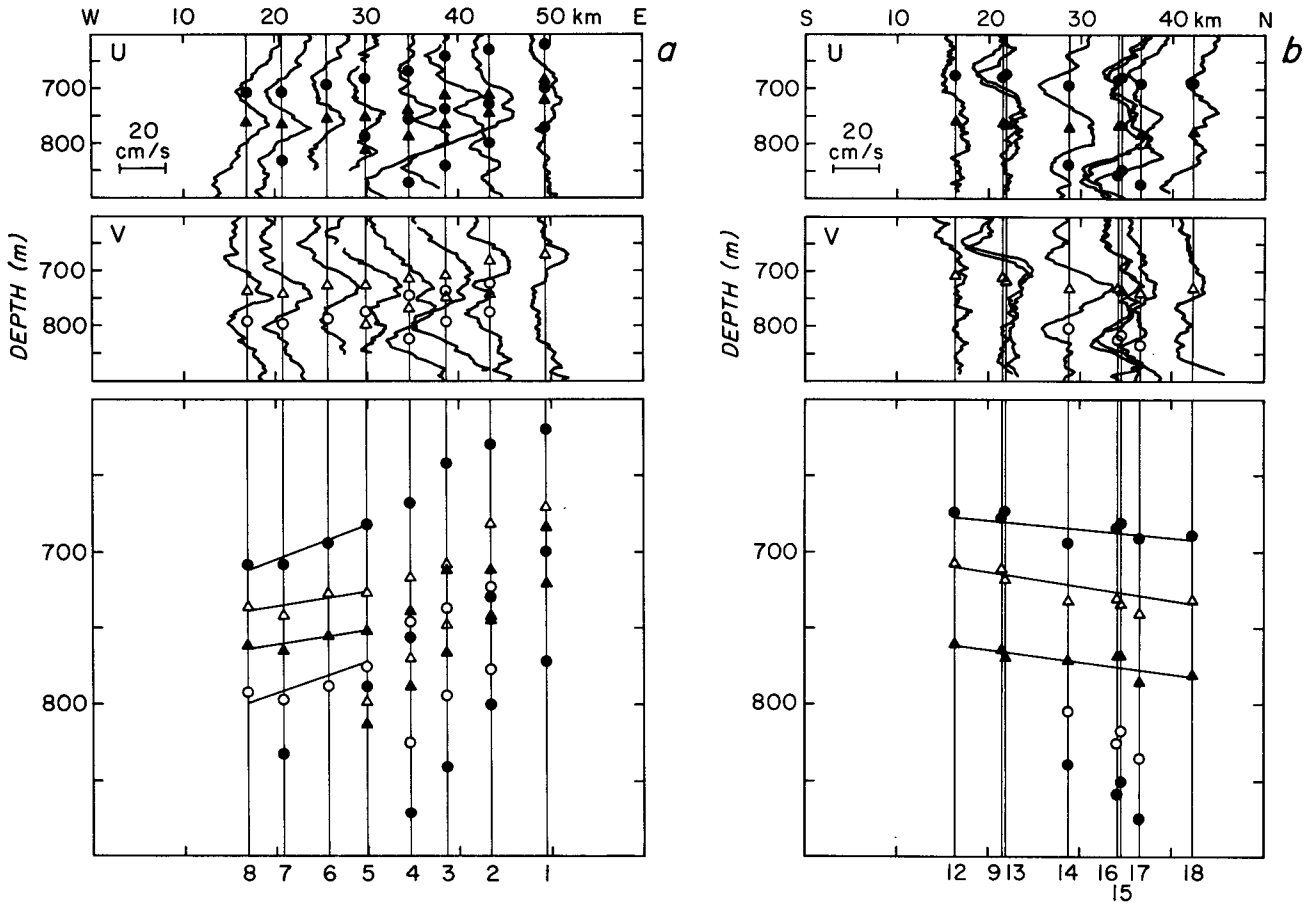

FIG. 9. Longitudinal (a) and meridional (b) sections of rotated velocity profiles in the energetic wavepacket. The east and north velocity components are plotted in the upper and middle panels, respectively. Wave crests are indicated by the symbols. These are combined in the bottom panel. The crests deepen to the west (a) and slightly to the north (b). The accompanying Table 3 gives the vertical and horizontal wavelengths, and Doppler shifts that can be computed from the spatial structure, as well as values after averaging each profile. For the longitudinal section, the estimates are based on crests west of XCP 104 only for reasons given in the text. The error bounds are 95% confidence limits computed with the bootstrap method (Efron and Gong, 1983).

not all taken at exactly the same location (Fig. 1). If the wave's extrema slope in space ($\Delta z/\Delta x$, $\Delta z/\Delta y$) as well as in time, spatial separations will contaminate the estimate of ω. This possibility will be explored after rotating the profiles to a common time to examine the spatial structure of the packet.

Figure 9 displays the rotated sections. A rotation frequency of $\omega = 0.8f$ consistent with the AVP results

TABLE 3. Vertical and horizontal wavelengths, and Doppler shift estimated for individual peaks and troughs and for profile ensembles (the extrema depths in each profile were averaged together before computing the horizontal wavelength) in sections XCP 105–108 (Fig. 9a) and XCP 112–118 (Fig. 9b).

	(a) East wavelength			(b) North wavelength		
	λ_z (m)	λ_x (km)	k_xU (f)	λ_z (m)	λ_y (km)	k_yV (f)
Solid circle	170 ± 40	−70 ± 20	−0.17 ± .04	160 ± 30	240 ± 140	0.01 ± .01
Open triangle	120 ± 10	−160 ± 340	−0.06 ± .09	180 ± 10	30 ± 2400	0.02 ± .01
Solid triangle	90 ± 30	−80 ± 90	−0.18 ± .15	180 ± 20	290 ± 730	0.01 ± .01
Open circle	100 ± 40	−60 ± 170	−0.34 ± .38			
Ensemble	*120 ± 20*	*−70 ± 40*	*−0.18 ± .09*	*170 ± 10*	*200 ± 170*	*0.01 ± .01*

was used. The accompanying Table 3 describes various wave parameters and their confidence limits estimated from the sections. Errors in the phase slopes $\Delta z/\Delta x$ and $\Delta z/\Delta y$ resulting from use of an inaccurate rotation frequency, namely $0.8(\pm 0.05)f$, should be less than 5% as each section took less than 3 h (or 0.15 inertial period) to deploy.

The longitudinal section (Fig. 9a) reveals that the points of inflection slope downward to the west. The wavevector **k** and phase velocity **C** are perpendicular to these lines of constant phase. For internal waves, the group velocity **C**g (direction of energy propagation) is parallel to these phase lines. Since we know this wave packet's energy is propagating downward from its clockwise-with-depth velocity structure, the downward slope to the west implies energy propagation to the west. In the eastern part of Fig. 9a, an energetic wave of smaller vertical wavelength appears to be superimposed on a larger scale wave while to the west only the larger wave is present. Both estimates of ω were in the region where the larger wave dominates. Therefore, we shall base estimates of the wave's properties solely on extrema west of XCP104. In the depth range of interest, vertical wavelengths λ_z range from 95 to 125 m, horizontal wavelengths λ_x from 60 to 160 km. Perturbations of the intrinsic frequency ω_0 from the lower bound of the internal waveband by either $N^2S_x^2/2f$ or $-S_x\partial V/\partial z$, where $S_x = -\Delta z/\Delta x$ $(=k_x/k_z)$, are at most $0.01f$. The Doppler shift (k_xU), on the other hand, is substantial, ranging from -0.06 to $-0.3f$.

The latitudinal section (Fig. 9b) reveals a more gently sloping phase. A single wave appears to dominate in this transect. The vertical wavelength λ_z ranges from 160 to 180 m, horizontal wavelength λ_y from 230 to 290 km. Contributions to the intrinsic frequency, $N^2S_y^2/2f$ and $S_y\partial U/\partial_z$, are even smaller than in the east–west section, less than $0.01f$. The Doppler shift k_yV is less than $0.02f$.

At this stage, we can consider possible errors in estimating ω from Fig. 8 due to the spatial separations of the profiles at the AVP sites and the horizontal phase slope $\Delta z/\Delta x$; the north–south slope $\Delta z/\Delta y$ is small enough to be ignored. The downslope to the west is such as to make the estimates at the two sites more alike but can account for at most $0.07f$, or 1/3, of the disparity. What remains, however, is within measurement noise.

The dispersion relation (1) can be expressed as

$$\omega = f + \zeta/2 + \gamma + k_xU + k_yV \qquad (2)$$

where $\gamma = \omega_0 - f_{\text{eff}}$. Our best estimates of the Eulerian frequency ω is $0.8(\pm 0.05)f$, of the Doppler shift contributions are $-0.15(\pm 0.06)f$ and $0.02(\pm 0.01)f$ for k_xU and k_yV, and of the intrinsic frequency anomaly γ is $0.01(\pm 0.01)f$. From Fig. 7, the vorticity of the core in the 18°C water above the wave packet is $-0.7(\pm 0.3)f$; however, its magnitude diminishes rapidly at the edge of the eddy (where most of the profiles containing the energetic wave are present) and also weakens with depth, under our assumptions vanishing between 800 and 900 m. Since it can be neglected within our confidence limits in (2), we conclude that the vorticity ζ makes no significant contribution to the dispersion relation. The balance is principally between the Eulerian frequency ω, the Coriolis frequency f and the x-component of the Doppler shift k_xU. The Eulerian frequency ω is below the Coriolis frequency f as a consequence of a negative Doppler shift acting on a near-inertial wave packet with intrinsic frequency $\omega_0 = 1.01(\pm 0.01)f$.

The proximity of the intrinsic frequency ω_0 to f as compared to the previous best estimate of the inertial peak intrinsic frequency of $\omega_0 = 1.05f$ from a region of little geostrophic shear (D'Asaro and Perkins, 1984) favors our hypothesis that the wave is encountering a critical layer. The dominance of the Doppler shift term suggests that intensification is a consequence of the mean flow shifting the intrinsic frequency ω_0 downward toward f. We conclude that critical-layer amplification due to the mean flow is responsible for the anomalous feature at the base of the eddy.

5. Summary and conclusions

Velocity measurements in the northwestern edge of the Sargasso Sea on and around Caryn Seamount revealed a surface-intensified anticyclonic eddy that appeared connected to the topography in much the same way as eddies found at the Corner Rise seamounts (Richardson, 1980). Internal wave energy levels were far below canonical GM values with the exceptions of an energetic downward-propagating near-inertial wave packet found at the base of the eddy and excess upward-propagating energy immediately above the summit.

Mean flow in the upper ocean was dominated by a warm mesoscale eddy over the southwest edge of the seamount. The eddy field was better modeled as a stationary feature than one being advected past the seamount by the impinging eastward flow. The eddy may result from vortex stretching as the ambient current flows over the peak experiment or may have formed when the Gulf Stream passed over the seamount between April and June 1978.

The energetic downgoing packet at the base of the eddy had vertical wavelengths of 120–170 m and a horizontal wavelength of 70 km. Its intrinsic frequency ω_0 was not measurably different from f while its Eulerian frequency $\omega = \omega_0 + (\mathbf{k}\cdot\mathbf{V})$ was $0.8f$. It was argued that this wave was undergoing critical-layer amplification. Critical-layer trapping of near-inertial waves can occur when depth variations of the mean flow Doppler-shift the intrinsic frequency down toward f (Olbers, 1981) or the vorticity cause the lower bound of the internal waveband, $f_{\text{eff}} = f + \zeta/2$, to rise toward the intrinsic frequency (Kunze, 1985). Doppler-shifting appears to be responsible here unlike previous obser-

vations (Kunze and Sanford, 1984) where vorticity trapping was implicated. The vorticity may, however, have played a role at shallower depths. It should be noted that this trapping appears to have occurred despite the wave scale being comparable to the size of the eddy. Under these conditions Olbers (1981) argues that the WKB approximation used in the wave-mean flow interaction models is no longer valid and the theoretical predictions therefore suspect.

The excess upgoing near-inertial energy on the peak's summit could have resulted from either topographic generation or reflection off the sloping bottom (Eriksen, 1982). Evidence favors the reflection hypothesis.

This study has provided additional evidence for critical-layer trapping and amplification of near-inertial waves in mean flow. Observations to date indicate that away from direct sources, such as in the surface mixed layer under storms, energetic near-inertial oscillations are the result of interactions with the mean flow. Earlier studies using moored current meters (e.g., Ruddick and Joyce, 1979; Brown and Owens, 1981) found near-inertial motions to be largely uncorrelated with the mean flow. This may be in part because the region of amplification spans a limited depth range O(100 m) which could easily be missed by widely spaced current meters on a mooring. Another confounding influence is that amplification occurs for negative vorticity or propagation against the flow, while waves are dispersed and energy levels reduced for positive vorticity or propagation with the flow. Thus, two contrary tendencies can both result from wave–mean flow interactions.

Enhanced internal wave energy is expected to lead to greater production of turbulence and mixing, particularly when accompanied by smaller vertical scales as is the case for both critical-layer processes and reflection off a sloping bottom. The two processes described here may then be important sinks of internal wave energy, one in the ocean interior and the other in the benthic bottom layer. Since the eddy that traps the inertial wave is itself connected to the seamount, topography's influence on mixing extends well into the interior. Past studies of mixing have been conducted with the assumption that mixing occurs uniformly and randomly in the ocean interior and studies of benthic turbulence have been mostly inferred based on larger scale features. This study suggests that greater effort should be concentrated in regions of mean flow where critical layers are expected and near sloping topography. At critical-layer sites, patches of microstructure activity would appear throughout the region of enhanced vertical shear. Given the scale of the packet observed here, this suggests enhanced turbulence levels spanning tens of meters in the vertical and kilometers in the horizontal. Measurements of turbulence made in a near-inertial feature by Gregg et al. (1986) are consistent with these scales. Lueck and Osborn (1985) found an even thicker region of excessive turbulent dissipation (over 100 m) below the thermostad in the core of a warm-core ring. Enhanced near-inertial waves have been observed in this same region of other warm rings (Kunze and Sanford, 1984b; Lueck, personal communication, 1985). These measurements suggest that shear instability does not occur in the form of a large overturning event involving the whole wave. Instead, its shear creates persisting conditions under which small perturbations are unstable.

Acknowledgments. The authors wish to thank ONR for financial support for the XCPs and analysis. The experiment was conducted under NSF support at the end of our AVP studies in the Local Dynamics Experiment of POLYMODE. We would like to thank an anonymous reviewer for pointing out the relevance of Eriksen's (1982) work to our results and inconsistencies in previous arguments favoring bottom generation of internal waves.

REFERENCES

Bell, T. H., 1975: Topographically generated internal waves in the open ocean. *J. Geophys. Res.*, **80,** 320–327.

Brown, E. C., and W. B. Owens, 1981: Observations of the horizontal interactions between the internal wave field and the mesoscale flow. *J. Phys. Oceanogr.*, **11,** 1474–1481.

D'Asaro, E. A., 1984: Wind forced internal waves in the North Pacific and Sargasso Sea. *J. Phys. Oceanogr.*, **14,** 781–794.

——, and H. Perkins, 1984: A near-inertial wave spectrum for the Sargasso Sea in late summer. *J. Phys. Oceanogr.*, **14,** 489–505.

Defant, A., 1961: *Physical Oceanography, Vol. 1.* Pergamon Press, 468–475.

Efron, B., and G. Gong, 1983: A leisurely look at the bootstrap, the jackknife and cross-validation. *Amer. Stat.*, **37,** 36–48.

Eriksen, C. C., 1982: Observations of internal wave reflection off sloping bottoms. *J. Geophys. Res.*, **87,** 525–538.

Fu, L.-L., 1981: Observations and models of inertial waves in the deep ocean. *Rev. Geophys. Space Phys.*, **19,** 141–170.

Gould, W. J., R. Hendry and H. E. Huppert, 1981: An abyssal topographic experiment. *Deep-Sea Res.*, **28,** 409–440.

Gregg, M. C., E. A. D'Asaro, T. J. Shay and N. Larson, 1986: Observations of persistent mixing and near-inertial internal waves. *J. Phys. Oceanogr.*, (in press).

Henderschott, M., 1973: Inertial oscillations of tidal period. *Progress in Oceanography,* Vol. 6, Pergamon, 1–27.

Johnson, C. L., and T. B. Sanford, 1980: Anomalous behavior of internal gravity waves near Bermuda. *J. Phys. Oceanogr.*, **10,** 2021–2034.

——, J. C. Van Leer and C. N. K. Mooers, 1976: A Cyclosonde view of coastal upwelling. *J. Phys. Oceanogr.*, **6,** 556–574.

Kunze, E., 1985: Near-inertial wave propagation in geostrophic shear. *J. Phys. Ocenogr.*, **15,** 544–565.

——, and T. B. Sanford, 1984: Observations of near-inertial waves in a front. *J. Phys. Oceanogr.*, **14,** 566–581.

Leaman, K. D., 1976: Observations of the vertical polarization and energy flux of near-inertial waves. *J. Phys. Oceanogr.*, **6,** 894–908.

——, and T. B. Sanford, 1975: Vertical energy propagation of inertial waves: a vector spectral analysis of velocity profiles. *J. Geophys. Res.*, **80,** 1975–1978.

Lueck R. and T. Osborn, 1985: The dissipation of kinetic energy in a warm-core ring. *J. Geophys. Res.*, (in press).

Magaard, L., 1968: Ein Beitrag zur Theorie der internen Wellen als storungen geostrophischer Stromungen. *Dtsch. Hydrogr. Z.*, **21,** 241–278.

Mied, R. P., C. Y. Shen, C. L. Trump and G. J. Lindemann, 1986:

Internal-inertial waves in a Sargasso Sea Front. Submitted to *J. Phys. Oceanogr.*

Mooers, C. N. K., 1975: Several effects of a baroclinic current on the cross-stream propagation of inertial-internal waves. *Geophys. Fluid Dyn.*, **6**, 245–275.

Munk, W., 1981: Internal waves and small scale processes. *Evolution of Physical Oceanography*, B. A. Warren and C. Wunsch, Eds., The MIT Press, 623 pp.

Olbers, D. J., 1981: The propagation of internal waves in a geostrophic current. *J. Phys. Oceanogr.*, **11**, 1224–1233.

Owens, W. B., and N. G. Hogg, 1980: Oceanic observations of stratified Taylor columns near a bump. *Deep-Sea Res.*, **27A**, 1029–1045.

Pinkel, R., 1983: Doppler sonar observations of internal waves. *J. Phys. Oceanogr.*, **13**, 804–815.

Richardson, P. L., 1980: Anticyclonic eddies generated near the Corner Rise seamounts. *J. Mar. Res.*, **38**, 673–686.

Roden, G. I. and B. A. Iaft, 1984: Effect of the Emperor Seamounts on the mesoscale thermohaline structure during the summer of 1982. *J. Geophys. Res.*, **90**, 839–855.

Ruddick, B. R., and T. M. Joyce, 1979: Observations of interaction between the internal wave field and low frequency flows in the North Atlantic. *J. Phys. Oceanogr.*, **9**, 498–517.

Sanford, T. B., R. G. Drever, J. H. Dunlap and E. A. D'Asaro, 1982: Design, operation and performance of an expendable temperature and velocity profiler (XTVP). Tech. Rep. 8110, Applied Physics Laboratory, University of Washington, Seattle, 83 pp.

——, —— and ——, 1985: An acoustic Doppler and electromagnetic velocity profiler. *J. Atmos. Oceanic Tech.*, 110–124.

Swaters, G. E., and L. A. Mysak, 1985: Topographically induced baroclinic eddies near a coastline with application to the Northeast Pacific. *J. Phys. Oceanogr.*, **15**, 1470–1485.

Weller, R. A., 1985: Near surface velocity variability at inertial and subinertial frequencies in the vicinity of the California Current. *J. Phys. Oceanogr.*, **15**, 372–385.

Worthington, L. V., 1959: The 18° water in the Sargasso Sea. *Deep-Sea Res.*, **5**, 297–305.

Wunsch, C., and S. Webb, 1979: The climatology of deep ocean internal waves. *J. Phys. Oceanogr.*, **9**, 235–243.